Faculty and Researchers   Faculty and Researchers' Publications

2019

River Discharge and Bathymetry Estimation from Inversion of Surface Currents and Water Surface Elevation Observations

Simeonov, Julian A.; Holland, K. Todd; Anderson, Steven P.

American Meteorological Society (AMS)

River Discharge and Bathymetry Estimation from Inversion of Surface Currents and Water Surface Elevation Observations

Julian A. Simeonov and K. Todd Holland

Marine Geosciences Division, Naval Research Laboratory, Stennis Space Center, Mississippi

Steven P. Anderson

Areté Associates, Arlington, Virginia

ABSTRACT

We developed an approach for estimating river discharge and water depth from measurements of surface velocity and water surface elevation, based on analytical velocity–depth and velocity–slope relationships derived from the steady gravity–friction momentum balance and mass conservation. A key component in this approach is specifying the influence of bottom friction on the modeled depth-averaged flow. Accordingly, we considered two commonly used bottom friction parameterizations—a depth-independent Darcy friction coefficient and a depth-dependent friction coefficient based on the Manning's roughness parameter. Assuming that the bottom friction coefficient is known, the unknown discharge was determined by minimizing the difference between the measured total head profile and the one determined from the velocity–slope relationship. The model performance and its sensitivity to key assumptions were evaluated using existing bathymetry data, and surface velocity and elevation observations obtained during field experiments on the Kootenai River near Bonners Ferry, Idaho, and the Hanford reach of the Columbia River. We found that the Manning's friction parameterization provided superior depth and discharge estimates, compared to the Darcy friction law. For both steady and moderately unsteady flow, inversions based on the Manning's friction provided discharge and thalweg depth estimates with relative errors not exceeding 5% and 12%, respectively.

1. Introduction

Recent interest in river depth estimation from remote sensing measurements of surface velocity or water surface elevation has resulted in a number of different hydrodynamic inversion methods (Zaron 2017). The inversions typically require knowledge of the discharge and the bottom friction, since the flow is inherently dependent on these parameters. While it is often assumed that the discharge and the friction are known a priori, these parameters cannot be easily sampled in situ or estimated from remote sensing measurements. Thus, for practical applications, it is important to develop approaches that simultaneously estimate depth, discharge, and bottom friction.

Currently, there are three main approaches to solving the depth inversion: 1) employ empirical relationships, 2) solve only the 1D dynamics of cross-stream averaged quantities, or 3) solve the full 2D depth-averaged shallow-water equations. Empirical Manning's resistance relationships between discharge, width, mean depth, and water slope were used successfully to estimate the discharge (Bjerklie et al. 2003) from remote sensing measurements of water surface elevation. This approach requires topography measurements and relies on in situ data to calibrate the unknown coefficients in the empirical relationships. Recently, Johnson and Cowen (2016) used particle image velocimetry (PIV) measurements of two-point correlations of surface velocity to demonstrate the existence of an empirical relationship between the integral length scale of turbulent eddies and the channel depth, thereby providing another means to remotely estimate the main channel depth.

Methods based on the 1D Saint-Venant equations were recently applied by Yoon et al. (2012; also Garambois and Monnier 2015) for estimation of discharge, the hydraulic depth, and the Manning friction coefficient from remote measurements of the water surface elevation; essential for this approach is time variation of the discharge.

Corresponding author: Julian A. Simeonov, julian.simeonov@nrlssc.navy.mil

These inversion approaches were motivated by an ongoing NASA effort to deploy a new Surface Water and Ocean Topography (SWOT) altimeter (Desai 2018) for global measurements of water surface elevation with an estimated 100-m resolution and 1-cm vertical accuracy.

An early 2D depth inversion approach was based on variational optimization and the adjoint method to efficiently minimize an error function between observations and predictions from a model based on the depth-averaged shallow-water equations (Honnorat et al. 2009). The approach was applied to determine joint topography and initial condition from Eulerian depth measurements and Lagrangian tracer trajectories using idealized bathymetry and simulated data. The assumed observation input in the above study consists of water depth measured in situ with drifters. Zaron et al. (2011) also used the adjoint method for variational assimilation of remotely sensed surface currents into the depth-averaged 2D shallow-water equations in order to predict bathymetry. Recently, several image-tracking techniques have been developed to estimate surface currents in riverine environments with 10–30-m spatial resolution from airborne IR imagery (Dugan et al. 2013) or satellite-borne multispectral imagery (Chen and Mied 2013). Using such surface velocity measurements for Haverstraw Bay on the Hudson River, Zaron et al. (2011) estimated the depth with rms errors of about 17% of the maximum depth. Almeida et al. (2018) also used the adjoint method and remote sensing measurements of the surface velocity to estimate the water depth over a 95-km length of the Columbia River at the Hanford reach with rms errors of about 11% of the maximum depth.

A different 2D depth estimation approach was based on a minimization of surface velocity errors using forward simulations over an ensemble of test bathymetries (Landon et al. 2014). Using drifter velocity measurements collected on the Kootenai River, Landon et al. (2014) estimated the river depth with 30% relative rms error for the maximum depth. Finally, we should note the approach of Gessese and Sellier (2012) that exploited the symmetry between bottom and surface elevation fields in the 2D shallow-water equations. In this approach, the equations are reformulated such that the forward model predicts depth and currents given the surface elevation field and boundary conditions consisting of upstream discharge and stage. Good results were obtained from identical twins forward and inverse numerical experiments. The approach has not been attempted with real observations of water surface elevations, which typically include measurement errors as well as spatial and temporal variability from 3D processes that are not included in the 2D model. As shown below, instantaneous surface elevation observations may contain regions where the total head downstream gradient is positive in the downstream direction and is therefore locally inconsistent with steady momentum balance.

There are a number of difficulties associated with the inversion of the unsteady shallow-water equations. It is well known (Bennett 2002) that the formal inversion of the shallow-water equations based on variational optimization leads to singular solutions because forcing observational solution values at interior points results in an ill-posed boundary value problem. To deal with the ill-posed boundary values, Gaussian weight functions and ad hoc regularization terms are introduced in the cost function to impose spatial correlations and to smooth the solution. As a result, the inverse solution is not unique but depends on the choice of somewhat arbitrary regularization parameters. Another difficulty with the inversion of the unsteady equations is that the spatiotemporal minimization of the cost function requires prohibitive amounts of synoptic velocity and surface elevation data inputs.

To avoid such difficulties, we pursue an analytical inversion approach based on the steady shallow-water equations. A distinct aspect of our approach is the utilization of stream-following coordinates, which provides the crucial simplification of the governing equations needed for analytical progress. Additionally, our approach provides simultaneous prediction of discharge and water depth, which should be contrasted with previous approaches that require the discharge as an input parameter. Among the previous works discussed above, there were only three studies (Landon et al. 2014; Zaron et al. 2011; Almeida et al. 2018) that used field observations to estimate real bathymetry; all of these studies used only velocity observations for the inversions. Here, we provide new bathymetry inversion results for the Kootenai River and the Columbia River that utilize both water surface elevation and surface currents observations. These observations are discussed in section 2. The simplified equations are presented in section 3a, where we also obtain an analytical inversion solution. The numerical implementation of the stream-following grid and the analytical inversion method is described in section 3b. The results of the test inversions and their sensitivity to data resolution and model assumptions are discussed in section 4.

2. Field sites and test data

a. Kootenai River

One of the field sites that will be used to test the inversion model is a 3-km region of the braided reach of the Kootenai River upstream of Bonners Ferry, Idaho
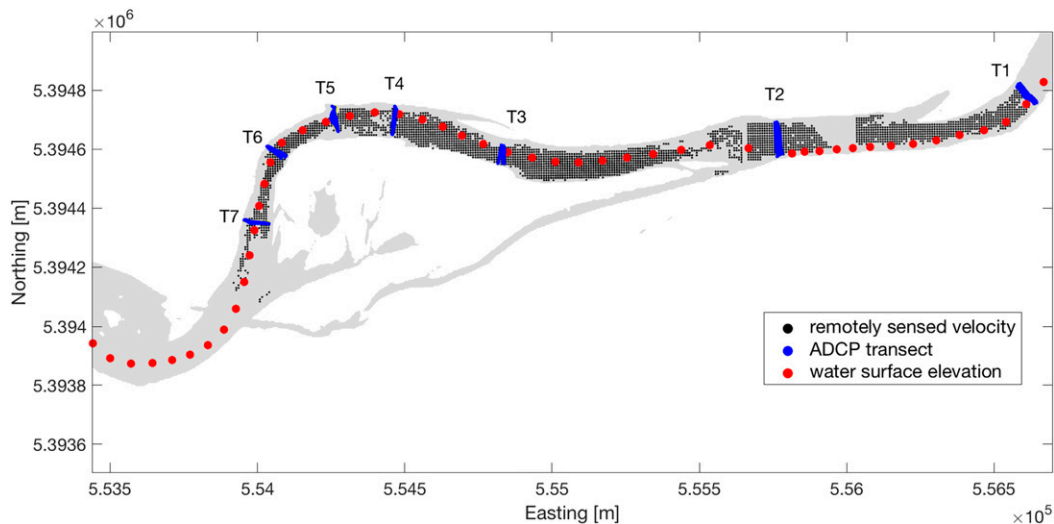
FIG. 1. A map of data points at the Kootenai River field site: remotely sensed surface velocity (black dots), ADCP velocity transects (blue), and water surface elevation (red circles) from upstream (T1) to downstream (T7). The coordinates are for Universal Transverse Mercator (UTM) zone 11, and the gray shading indicates area covered by water.

(Fig. 1). This reach of the river is characterized with gravel- and cobble-bed substrate with a median grain size $D_{50} = 39.9$ mm and a mean bed slope of 0.0046 (Barton 2004). The inversion tests for this site will use in situ and remote sensing hydrographic measurements collected by the Naval Research Laboratory (NRL), the Naval Postgraduate School (NPS), and Areté Associates as part of a field experiment conducted during 12–17 August 2010. NRL collected in situ velocity and discharge data with a towed ADCP at several transects shown in Fig. 1 (blue dots). The water surface elevation measured by temporary gauges and at the Leonia USGS station varied by less than 2 cm during the same period, indicating steady flow conditions. The average daily discharge measured by the ADCP was about $213 \, \mathrm{m^3 \, s^{-1}}$ with a typical uncertainty of about 5% ($\sim 10 \, \mathrm{m^3 \, s^{-1}}$). NPS collected instantaneous water surface elevation measurements using a drifting boat equipped with kinematic GPS (Fig. 1, red circles). The profile of the water surface elevation shown in Fig. 2 indicates a sequence of riffles and pools. Airborne IR imagery collected by Areté was used to derive surface currents on an 8 m × 8 m grid (Fig. 1, black dots). An example of the derived currents is shown in Fig. 3. The vertical velocity profiles measured with the ADCP were used to estimate the ratio of the surface velocity to the depth-averaged velocity [see Simeonov et al. (2013) for further details]. The estimated ratio of 0.79 was then used to convert the remotely sensed surface velocity to depth-averaged velocity that is needed for the inverse model. We should note that similar ADCP measurements in the meander reach of the Kootenai River downstream of Bonners

Ferry (not shown) yielded a ratio of 0.86 that was much closer to the theoretical value 0.85 suggested by Rantz (1982). The predicted water depths will be compared to depths inferred from the in situ water surface elevation and multibeam echo sounder bathymetry collected in 2009 by the U.S. Geological Survey (G. Barton 2010, personal communication). These bathymetry measurements were verified at multiple locations using single-beam sonars during the 2010 experiments to establish accurate water depths to be used in our analysis.

b. Columbia River

The second field site is an 80-km reach of the Columbia River (Fig. 4), located about 24 km downstream of the Priest Rapids Dam. NRL and Areté Associates conducted extensive in situ and remote sensing velocity measurements at this site during 5–8 October 2011. In situ measurements of the velocity vertical profiles were gathered on 5–7 October with a towed ADCP along 28 transects (Fig. 4, blue dots) by NRL. It was found that the ADCP data conform to a ratio of the surface velocity to the depth-averaged velocity equal to 0.84 with an R^2 value of 0.97. This value is also close to the theoretical value of 0.85.

The primary test data again consist of remotely measured surface currents (Fig. 4, black dots) collected by Areté between 0300 and 0610 PDT 8 October 2011 and water surface elevation recorded continuously at seven gauges (red circles) by the Pacific Northwest National Laboratory (PNNL). An offset of 1.038 m was used to change the water surface elevation data from the National Geodetic Vertical Datum of 1929 (NGVD29) to
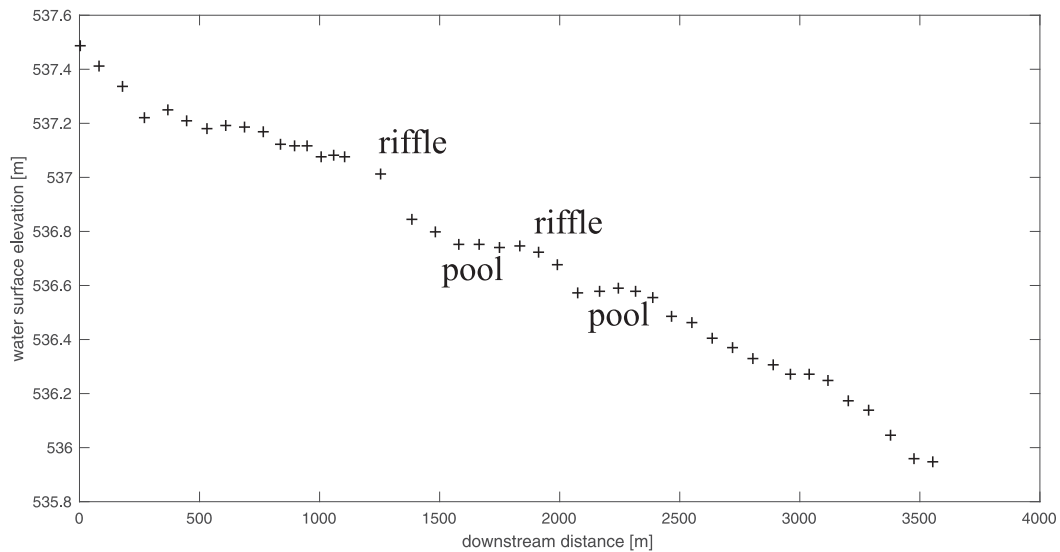
FIG. 2. The observed Kootenai River water surface elevation (NAVD88).

the North American Vertical Datum of 1988 (NAVD88). The time variation of the water surface elevation (Fig. 5) at five of the gauges shows $O(1)$-m fluctuations, which are the largest at a USGS gauge, and they tend to dampen further downstream. These surface elevation fluctuations were caused by power plant operations at the Priest Rapids Dam. The river discharge measured at the USGS gauge (Fig. 6) shows that the river flow at that location decreased from 2050 to $1200\,\mathrm{m^3\,s^{-1}}$ during the 0300–0600 PDT collection of
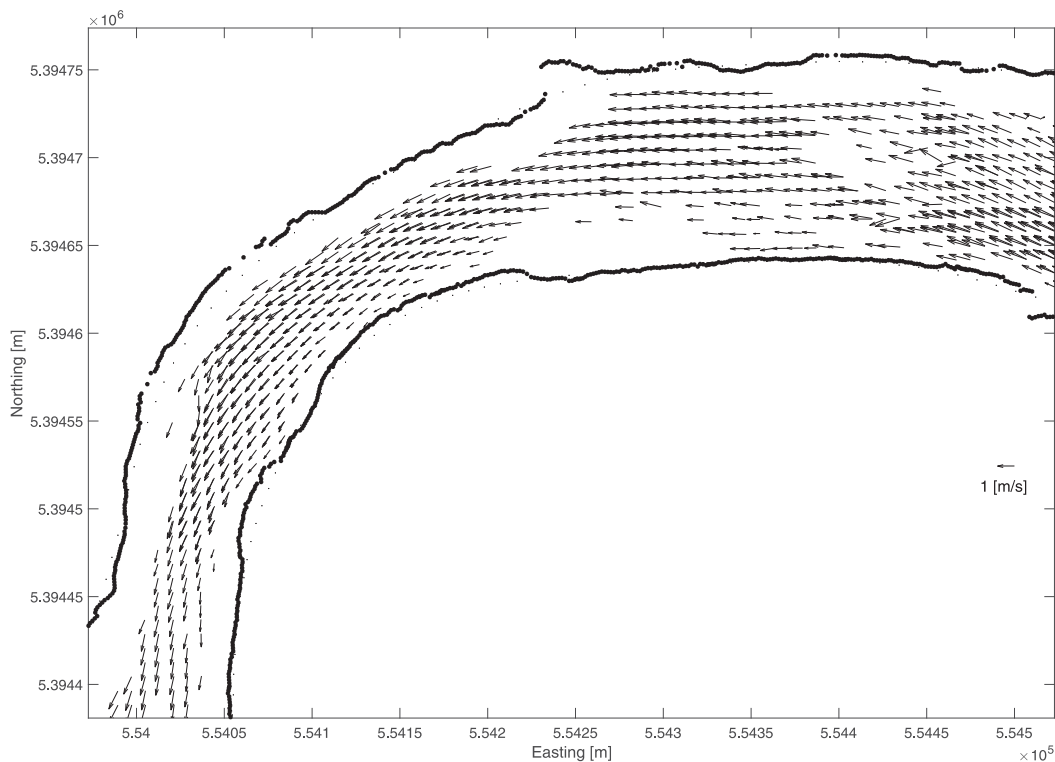

FIG. 3. Example of airborne IR-derived velocity measurements developed by Areté Associates from the Kootenai River field site (Fig. 1). The velocity estimates are computed on $8\,\mathrm{m} \times 8\,\mathrm{m}$ tiles.
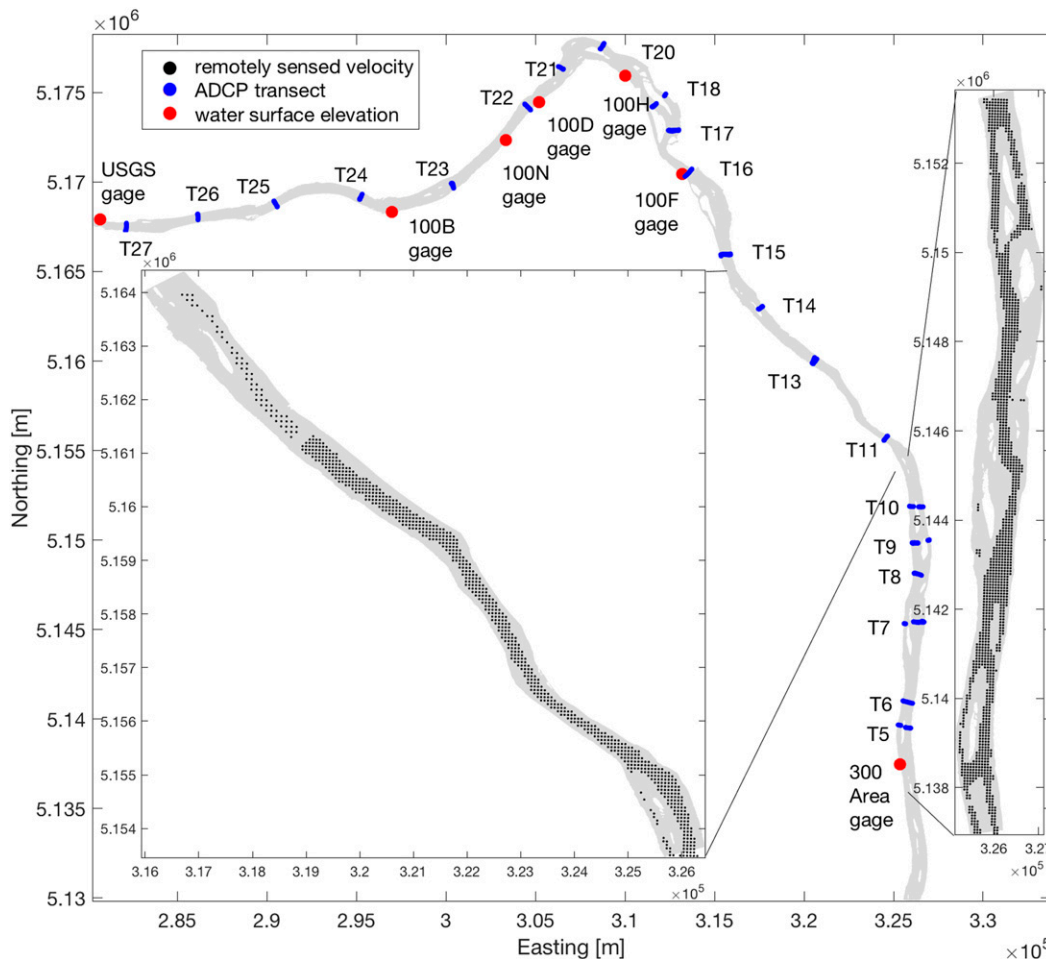
FIG. 4. A map of data points at the Columbia River field site: remotely sensed surface velocity (black dots in the two insets), ADCP velocity transects (blue), and water surface elevation (red circles) from upstream (T27) to downstream (T5). The coordinates are for UTM zone 11, and the gray shading indicates area covered by water.

the surface velocity data. We should point out that as a result of the unsteady nature of the flow, the local discharge throughout our 80-km reach would be significantly different from the one measured at the USGS gauge. While detailed measurements of the spatiotemporal variability of the discharge are not available, such information (Fig. 7) was provided by Marshall Richmond (PNNL, 2011, personal communication), who ran hindcast simulations with the Modular Aquatic Simulation System in Two Dimensions (MASS2) for conditions at 0300 and 0500 PDT 8 October 2011. The results in Fig. 7 indicate large discharge fluctuations in the upper half of the domain and less dramatic discharge variation farther downstream, where the discharge approaches some longer-term mean value in the range of 1500–1700 $m^3 s^{-1}$.

Both, the water surface elevation fluctuations and the discharge fluctuations are less pronounced in the lower half of the experimental site (Figs. 5 and 7). Therefore, our inversions for the Columbia River will be limited to the lower half of the field site, using an upstream boundary near ADCP transect 16. We further split the surface velocity data into two sets—0300–0415 and 0445–0610 PDT—to approximate the river conditions at 0300 and 0500 PDT, respectively. To account for the islands that are present in this reach, we augmented the Areté velocity dataset with zero-velocity data points over the islands. The 0500 PDT velocity data were estimated on a square grid with a grid size of about 96 m. The 0300 PDT velocity data were estimated on a 96-m grid upstream of transect T15 and a 65-m grid downstream of T15. For the purpose of inversions with our depth-averaged flow model, the Areté surface velocity data were converted to depth-averaged velocity using the above ADCP measured ratio of 0.84. We also used linear interpolation to estimate the water surface
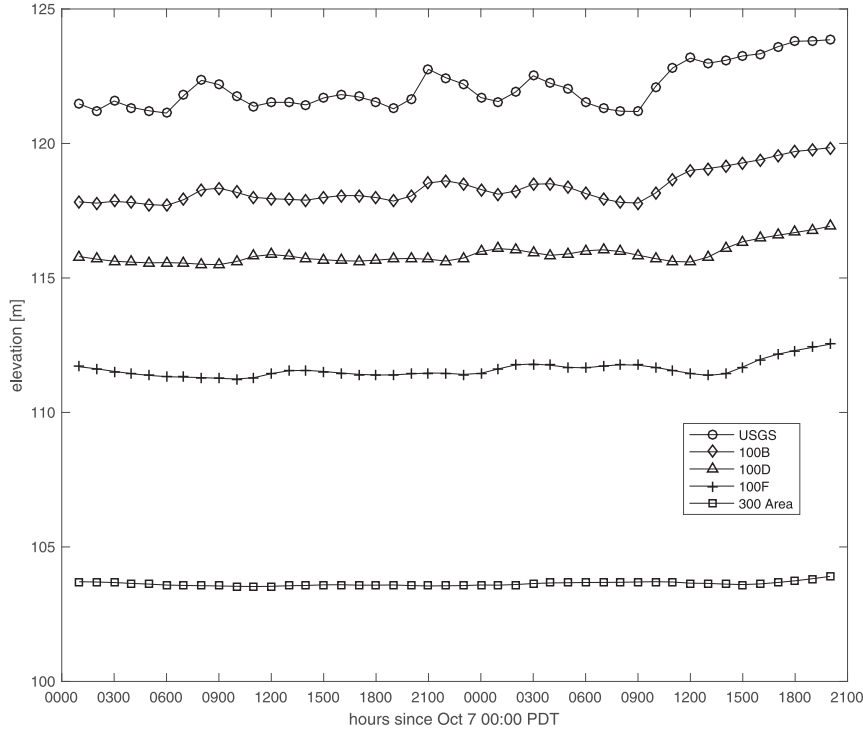
FIG. 5. Water surface elevation at five gauges: USGS (circles), 100B (diamonds), 100D (triangles), 100F (plus signs), 300 area (squares).

elevation between gauges. The depth estimation results presented in section 4 below were compared to a recent bathymetric dataset (Coleman et al. 2010) consisting of lidar and single-beam echo sounder measurements.

3. Methods

a. Analytical inversion of depth and discharge

The starting point for our inversion approach is the streamwise momentum balance for gradually varying open channel flow:

$$hgS = -C_D U^2, \qquad (1)$$

where h is the depth; U is the depth-averaged streamwise velocity component;

$$S = \frac{\partial}{\partial \eta}\left(\frac{U^2}{2g} + z_S\right) \qquad (2)$$

is the streamwise gradient of the total head $z_T = z_S + U^2/2g$; z_S is the surface elevation; g is gravity; η and ζ are the local downstream and cross-stream coordinates, respectively; and C_D is the bottom drag coefficient. Note that the depth could be easily estimated from (1) if we had reliable estimates of the steady-state total head slope from the

measurements of the water surface elevation and velocity. Unfortunately, real data contain noise and other unsteady processes that lead to regions with $S \geq 0$ that violate (1). Here, we pursue an approach where the steady-state total head slope is considered unknown, is spatially variable, and is determined as part of the inversion.

The feasibility of analytical inversion relies upon a number of simplifications to the model equations. The selection of a local reference frame (η, ζ) aligned with the streamlines is the primary simplification. Another simplification in the momentum balance equation, (1), results from neglecting momentum transfer by secondary flows and lateral mixing by turbulence, which are expected to be important only near the channel lateral boundaries. The small dynamic contribution $U^2/2g$ to the total head can also usually be neglected in low steepness channels, but it is retained, since the Kootenai River test case is a steeper stream characterized with riffle-pool series. A related simplifying assumption is that the total head is cross-channel uniform, in which case a simple finite difference estimate of the total head slope,

$$S(\eta, \zeta) = \frac{\Delta z_T(\eta)}{\Delta \eta(\zeta, \eta)}, \qquad (3)$$

implies that the ζ variation of the local total head slope is just the result of the ζ variation of the downstream
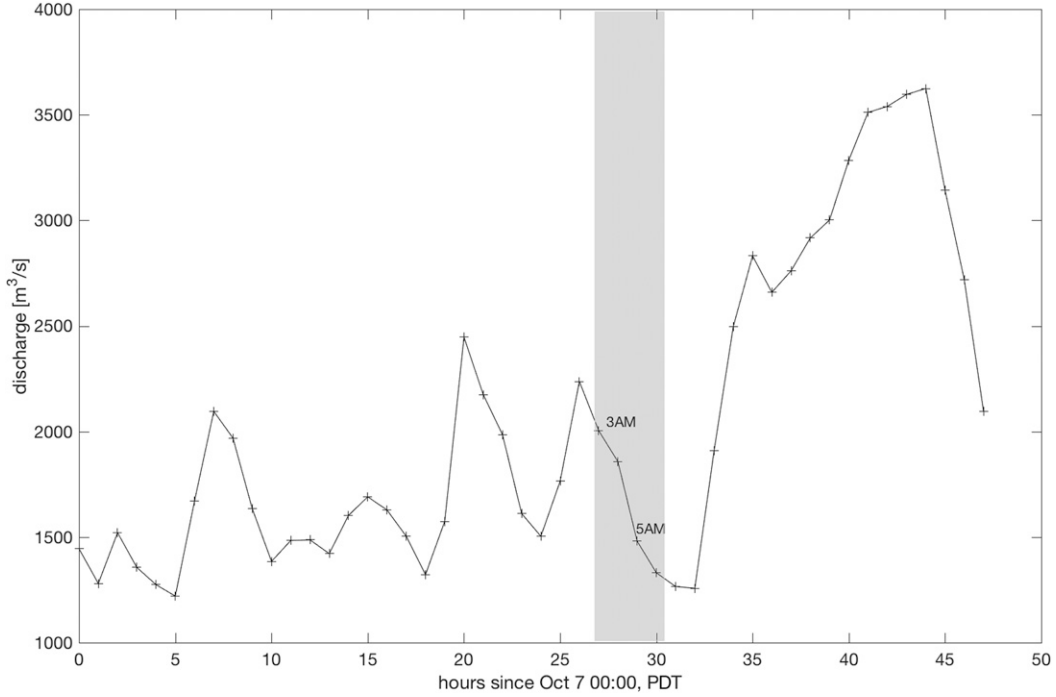
FIG. 6. Discharge measured at the Columbia River USGS gauge station (Fig. 4, red dots). The shaded interval corresponds to the time of the airborne IR imagery collection.

distance $\Delta\eta$ between the two total head levels separated by Δz_T (i.e., the total head slope is reduced near the outer bank of a bend). The ζ average of (3) then allows us to express S in terms of its ζ average $\overline{S}$, defined as

$$S(\eta,\zeta) = \frac{\overline{S}(\eta)}{\Delta\eta_0(\zeta,\eta)}, \tag{4}$$

and a simple factor,

$$\Delta\eta_0(\zeta,\eta) = \frac{\Delta\eta}{\overline{\Delta\eta}}, \tag{5}$$

that is a known function of the local channel curvature/geometry. In the following, we will use ζ_R and ζ_L to denote the coordinates of the right and left shorelines, respectively.

For constant depth-independent bottom friction C_D and constant discharge Q, mass conservation

$$Q = \int_{\zeta_L}^{\zeta_R} hU \, d\zeta = \text{const} \tag{6}$$

and (1) and (4) yield the following velocity–slope relationship:

$$\overline{S}(\eta) = -\frac{C_D}{gQ} I, \tag{7}$$

where

$$I(\eta) = \int_{\zeta_L}^{\zeta_R} \Delta\eta_0 U^3 \, d\zeta \tag{8}$$

is a 1D function that is completely determined by the velocity observations and the channel geometry. Integrating (7), the depth-independent bottom friction (also known as Darcy) model results in the following prediction for the total head:

$$\overline{z}_{\text{mod}}(\eta) = \overline{z}_{\text{mod}}(\eta_{\text{up}}) - \frac{C_D}{gQ}\int_{\eta_{\text{up}}}^{\eta} I \, d\eta. \tag{9}$$

When (7) and (4) are used to eliminate the slope S from (1), we obtain the following velocity–depth relationship, where the only unknown parameter is the discharge

$$h = \frac{\Delta\eta_0 Q U^2}{I}. \tag{10}$$

It is also commonly assumed that the bottom friction depends inversely on the one-third power of the water depth,

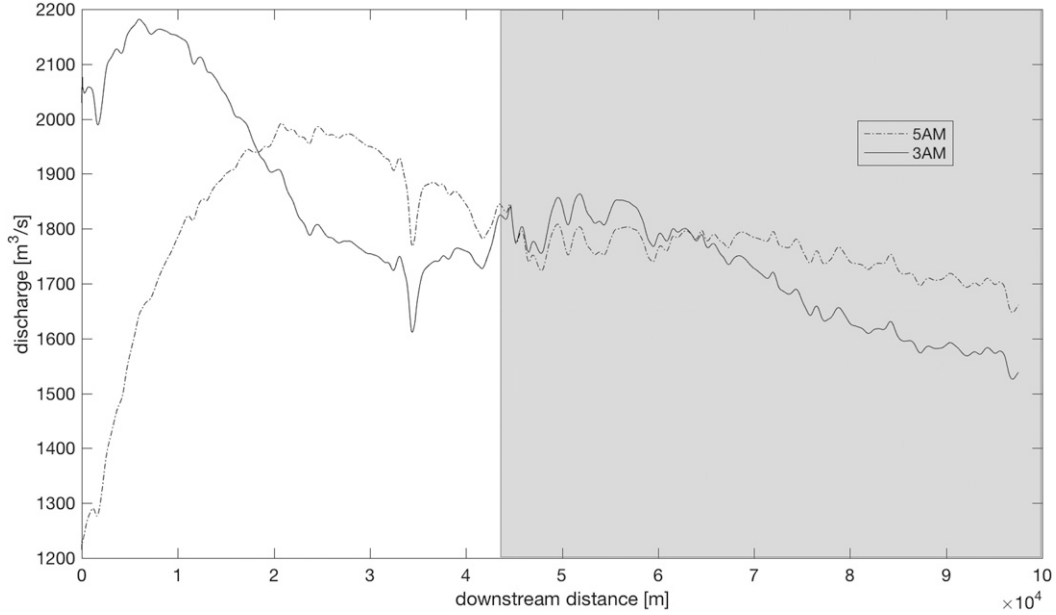$$C_D = \frac{gn^2}{h^{1/3}}, \tag{11}$$

FIG. 7. Local discharge along the Columbia River site at 0300 and 0500 PDT predicted by PNNL with the MASS2 model. The shading denotes the region with quasi-steady discharge suitable for our steady-state inversion model.

where n is the Manning's roughness coefficient. For this Manning's friction model, the momentum balance equation, (1), becomes

$$h = \left(-\frac{n^2}{S}\right)^{3/4} U^{3/2}. \qquad (12)$$

Using the momentum balance equation, (12); mass conservation equation, (6); and the slope estimate equation, (4), we obtain the following velocity–slope relationship for the Manning's friction model:

$$\overline{S}(\eta) = -\frac{n^2}{Q^{4/3}} I_n^{4/3}, \qquad (13)$$

where

$$I_n(\eta) = \int_{\zeta_L}^{\zeta_R} \Delta \eta_0^{3/4} U^{5/2} \, d\zeta. \qquad (14)$$

Integrating (13), the Manning's friction model yields the following prediction for the total head:

$$\overline{z}_{\text{mod}}(\eta) = \overline{z}_{\text{mod}}(\eta_{\text{up}}) - \frac{n^2}{Q^{4/3}} \int_{\eta_{\text{up}}}^{\eta} I_n^{4/3} \, d\eta. \qquad (15)$$

Finally, using (13) and (4), the momentum balance equation, (12), yields the following explicit velocity–depth relationship for the Manning's friction model:

$$h = \frac{\Delta \eta_0^{3/4} Q U^{3/2}}{I_n}. \qquad (16)$$

Assuming that the bottom roughness (given by C_D or n) is known, the equations for velocity–depth, (10) and (16), and velocity–slope, (7) and (13), indicate that the inverse solution depends on the unknown discharge Q. Here, we adopt an approach that estimates the unknown discharge by fitting the predicted mean total head, (9) or (15), to the respective ζ average of the measured total head field $\overline{z}_{\text{obs}}(\eta) = \int_{\zeta_L}^{\zeta_R} z_T(\zeta, \eta) \, d\zeta$.

Three different discharge fitting schemes are considered, depending on whether the predicted total head elevation is forced to match the observed one at the upstream and downstream endpoints. The simplest scheme, referred to as *fixed endpoints*, is obtained by setting the predicted total head equal to the observed one at both the upstream and downstream endpoints. Equations (9) and (15) then give the following simple estimates for the discharge:

$$Q = \frac{-C_D \int_{\eta_{\text{up}}}^{\eta_{\text{down}}} I \, d\eta}{g[\overline{z}_{\text{obs}}(\eta_{\text{down}}) - \overline{z}_{\text{obs}}(\eta_{\text{up}})]} \qquad (17a)$$
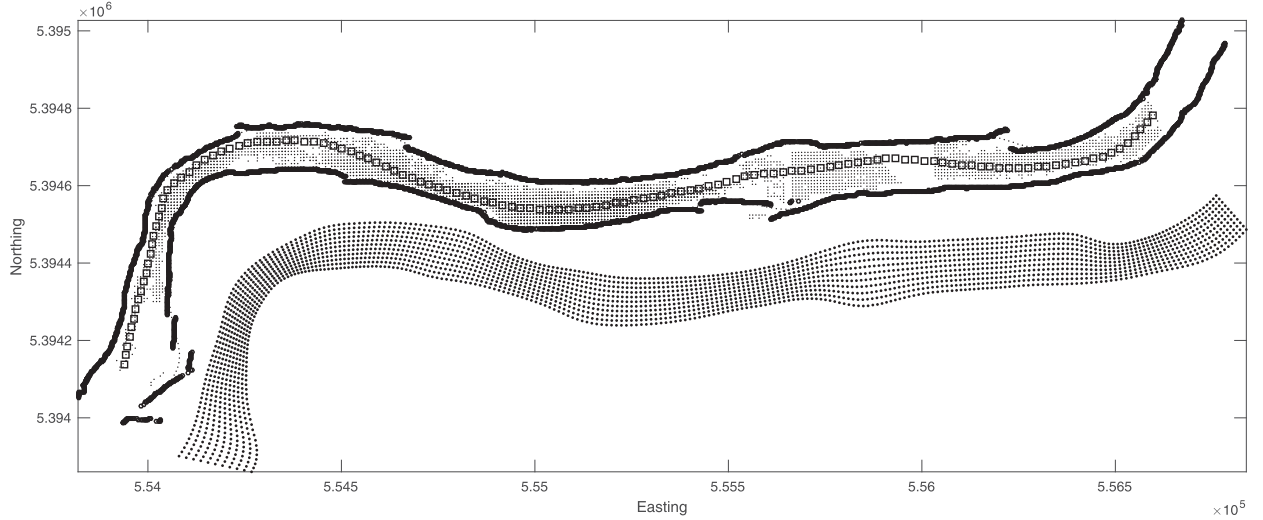
and

FIG. 8. Example of curvilinear grid (bottom image) generation for the Kootenai River site using the shorelines (bold circles) and a maximum velocity streamline (squares). The grid is shown with an easting and northing offsets of 200 and −250 m, respectively. The streamline is generated by integrating the IR-image–derived velocity measurements (Fig. 1, black dots).

$$Q^{4/3} = \frac{-n^2 \int_{\eta_{\text{up}}}^{\eta_{\text{down}}} I_n^{4/3}\, d\eta}{\overline{z}_{\text{obs}}(\eta_{\text{down}}) - \overline{z}_{\text{obs}}(\eta_{\text{up}})}, \qquad (17\text{b})$$

respectively. A downside of the fixed endpoints scheme is that it gives too much weight to the endpoint values of the total head and ignores its interior variations. To account for interior variations, we also use a least squares (LS) approach that minimizes $[\overline{z}_{\text{obs}}(\eta) - \overline{z}_{\text{mod}}(\eta)]^2$. We refer to this scheme as *fixed upstream LS* if we also enforce the condition $\overline{z}_{\text{mod}}(\eta_{\text{up}}) = \overline{z}_{\text{obs}}(\eta_{\text{up}})$. Alternatively, the modeled upstream and downstream total head is assumed to be unknown and is determined as part of the LS minimization; we refer to this scheme as *free endpoints LS*.

b. Numerical implementation

The hydrodynamic equation, (1), and the analytical approach described in the previous section require a streamline-following grid. We therefore need the shoreline coordinates to confine the numerical grid. The shorelines can be determined using feature extraction from images or using the intersection of the measured bathymetry with the known water surface elevation. In our results below, we have used the latter approach, which avoids the introduction of additional uncertainties associated with the shoreline determination from imagery. We construct a maximum velocity streamline (Fig. 8, squares) by choosing a starting point near the velocity maximum at the upstream end. The coordinate vector $\mathbf{r}_i = (\zeta_i, \eta_i)$ of subsequent points on the streamline is

determined by integrating the measured velocity field $\mathbf{u}^{\text{obs}}$ (Fig. 8, gray dots) as follows:

$$\mathbf{r}_{i+1} = \mathbf{r}_i + \Delta\eta \frac{\mathbf{u}^{\text{obs}}(\mathbf{r}_i)}{|\mathbf{u}^{\text{obs}}|}, \qquad (18)$$

where $\Delta\eta$ is a fixed distance increment comparable to the resolution of the measured velocity. Triangle interpolation of the measured data is used to estimate the velocity field at the location of the streamline points. Special care is used to increase the value of $\Delta\eta$ when the streamline integration encounters a small data gap. We construct the curvilinear grid (Fig. 8, bottom) by dividing the segment between the two shorelines into N_ζ equal intervals for each streamline point. The number of cross-channel nodes is the same for each downstream location, but the resulting cross-stream grid step varies in the downstream direction proportional to the river width. Once the streamline curvilinear grid is generated, the scattered velocity data points are interpolated onto the streamline grid and the cross-channel integrals in (8) and (14) are estimated using trapezoidal quadratures.

4. Results and discussion

Here, we present results of depth and discharge estimation, beginning with the easiest case of the Kootenai River, where the discharge was steady and the channel geometry was simple. We then consider the more difficult case of the Columbia River, where the discharge was temporally and spatially variable, and the channel geometry included multiple islands. The discharge
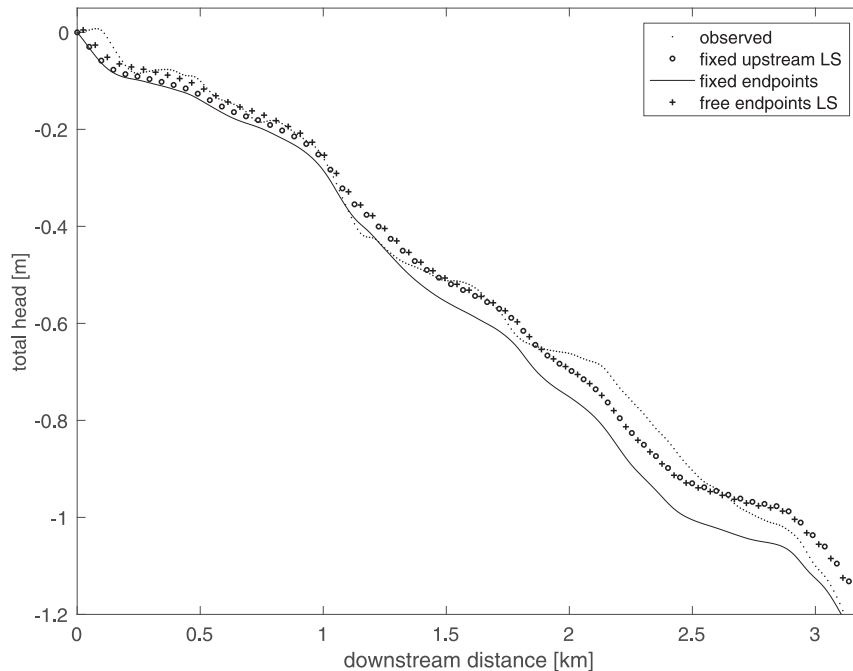
Fig. 9. Predicted and measured total head for the Kootenai River, offset by the measured total head at the upstream end.

estimation is evaluated using several different approaches to fit the predicted and the observed total head. We also investigate the sensitivity of the results to grid resolution, the geometric correction to the surface slope, and the assumed bottom friction parameterization.

a. Kootenai River: Constant discharge

We first consider inversions using depth-dependent bottom friction parameterization based on the Manning's roughness and a curvilinear grid with $N_\zeta = 10$ cross-channel steps and along-channel grid step $\Delta\eta = 14.5$ m. The Manning roughness value $n = 0.0275$ for the considered reach of the Kootenai River was determined from a friction coefficient $C_D = 0.005$ calibrated for the observed discharge $Q = 213$ m^3 s^{-1} (Simeonov et al. 2013) and an estimate of the mean thalweg depth $h_{TW} = 3.29$ m [see (11)] from the measurements. The predicted total head from the fixed endpoints scheme and the two LS schemes is compared in Fig. 9 against the observed total head. The figure shows that the two LS schemes provide much better approximation to the observed total head compared to the fixed endpoints scheme. Nevertheless, all three schemes were found to perform quantitatively well, with bias and rms errors less than 4 cm and R^2 values larger than 0.97 (Table 1). Table 1 shows that the two LS schemes slightly overestimate (by about 5% and 7%, respectively) the observed discharge

of $Q = 213$ m^3 s^{-1}, while the discharge from the fixed endpoints scheme is very close to the observed one.

The predicted spatial distribution of the water depth using the fixed endpoints scheme is compared in Fig. 10 against the measured depths. The figure demonstrates that the model is able to capture the observed patterns of shallow and deep areas of the river channel. Very similar water depth patterns (not shown) were obtained with the LS schemes. The 2D depth error statistics for all three total head minimization schemes (Table 1) indicate a negligible bias of about 10 cm, an rms error of about 80 cm, and an R^2 value of 0.59. For comparison, Landon et al. (2014) obtained a twice-smaller rms depth error for the same region using forward 2D simulations over an ensemble of test topographies. In addition to assuming that the discharge is known, the latter study used a different bottom friction coefficient $C_D = 0.0035$, included turbulent horizontal mixing with an eddy viscosity coefficient of 0.02 m^2 s^{-1}, and used regularization parameters such as a correlation length scale and a magnitude of the weight functions that forced the dynamical model toward the observations. The knowledge of such regularization parameters would be unrealistic for operational applications of bathymetry inversion.

While the overall prediction of the depth patterns in our model is good, there are notable deficiencies near the two bends where the predicted maximum depth is not as close to the bank as the observed maximum depth

TABLE 1. Inversion statistics for the Kootenai River data (12–17 Aug 2010) with average daily discharge $Q = 213 \, \mathrm{m^3 \, s^{-1}}$.

Minimization scheme	N_ζ	Predicted discharge $(\mathrm{m^3 \, s^{-1}})$	Total head (m)			Thalweg depth (m)			2D depth (m)		
			Bias	rms	R^2	Bias	rms	R^2	Bias	rms	R^2
Free endpoints LS	10	223	0	0.03	0.99	−0.04	0.60	0.73	−0.08	0.81	0.59
Fixed endpoints	10	214	−0.05	0.04	0.97	−0.16	0.59	0.72	−0.14	0.79	0.59
Fixed upstream LS	10	227	−0.01	0.03	0.99	0.03	0.61	0.73	−0.05	0.82	0.58
Free endpoints LS[a]	10	188	0	0.03	0.99	−0.32	0.60	0.67	−0.37	0.82	0.49
Fixed endpoints[a]	10	179	−0.05	0.04	0.97	−0.46	0.59	0.59	−0.43	0.81	0.47
Fixed upstream LS[a]	10	194	−0.01	0.03	0.99	−0.23	0.60	0.70	−0.33	0.83	0.50
Fixed endpoints[b]	10	214	−0.05	0.04	0.97	−0.17	0.61	0.71	−0.14	0.81	0.58
Fixed endpoints	20	216	−0.05	0.04	0.97	−0.22	0.63	0.70	−0.14	0.82	0.53
Fixed endpoints	5	214	−0.05	0.03	0.97	−0.16	0.60	0.70	−0.10	0.76	0.68

[a] Minimization schemes using the Darcy friction model instead of the Manning friction.
[b] Minimization that did not use the geometric correction to the total head slope.

(see Fig. 10). One possible reason for this deficiency is that the steep banks (i.e., large gradients in the depth) are not resolved in the velocity data because of the relatively large gaps near the banks (e.g., Fig. 3). The velocity data gaps near the banks resulted from the presence of tree shadows in the imagery.

To exclude the errors resulting from the bank data gaps, we also considered how the predicted thalweg depth compares to the observed one. Figure 11a shows that the three minimization schemes predict a very similar streamwise variation in the difference between the predicted and observed thalweg depths. The model skill of predicting the thalweg depths is further illustrated in Fig. 11b. All three minimization schemes have an rms thalweg depth error of about 60 cm and an R^2 value of about 0.73 (Table 1). The predicted thalweg depth with the fixed endpoints scheme has a somewhat larger negative bias of 16 cm compared to the $O(4)$-cm bias of the two LS schemes. Overall, the above results suggest that our inversion scheme is characterized with very low bias errors and 9%–11% relative rms errors (for a maximum depth of 7 m) that compare to the

typical measurement errors in the velocity data (Dugan et al. 2013; also Simeonov et al. 2013).

We also explored the sensitivity of these results to the assumed bottom friction law, the geometric correction to the surface slope, and the grid resolution. Using the same grid with $N_\zeta = 10$ cross-channel steps, Table 1 shows that the inversions based on the Darcy friction law predict discharges in the range of 179–$194 \, \mathrm{m^3 \, s^{-1}}$, which significantly underestimate the observed discharge. This deficiency of the Darcy friction model translates into an order of magnitude larger (negative) bias in the predicted water depths (Table 1). We conclude that the Manning's friction model is essential to obtain unbiased estimates of the water depth. An error analysis of (17a) and (17b) further suggests the following expressions: $\delta Q / Q = \delta C_D / C_D$ and $\delta Q / Q = 3 \delta n / 2n$, which relate the discharge error δQ to uncertainties in the friction coefficients δC_D and δn. The same relative error expressions also hold for the depth, which is linearly proportional to the discharge according to (10) and (16). Therefore, 10% uncertainties in C_D and n will result in 10% and 15% errors, respectively, in the predicted depth.
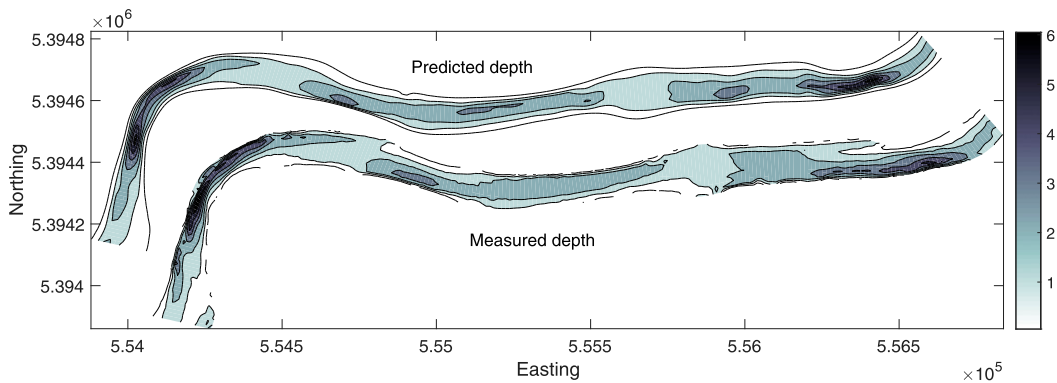

FIG. 10. Predicted and measured water depth map (blue shading) for the Kootenai River using the fixed-endpoint method. The measured depth map has easting and northing offsets of 200 and −250 m, respectively.
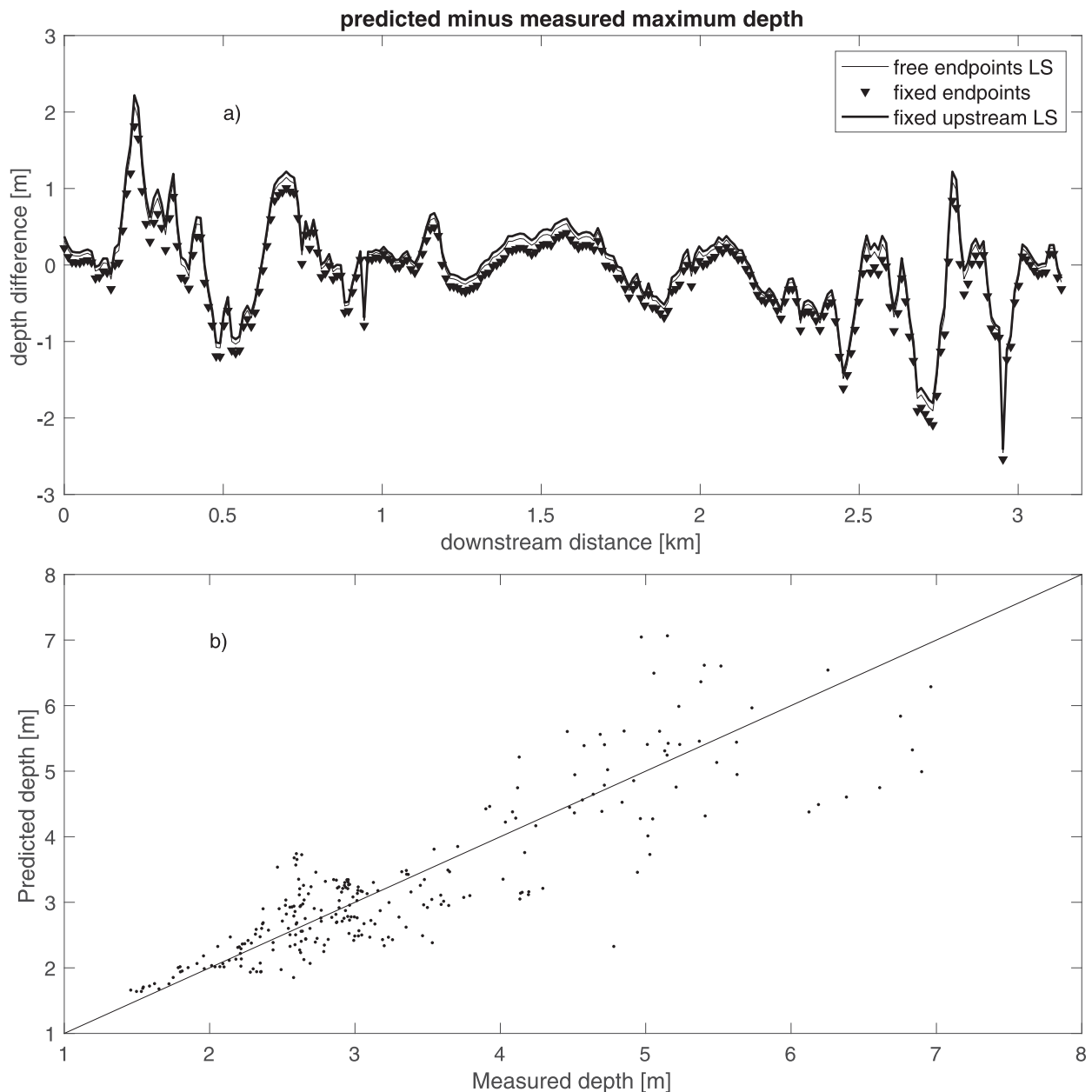
FIG. 11. (a) Difference between predicted and measured thalweg water depth for the Kootenai River site using different minimization schemes. (b) Predicted thalweg depth (dots) vs measured depth and the 1:1 line corresponding to perfect prediction; only the free-endpoints LS scheme is shown, since the other two schemes are similar.

The effect of the geometric correction was investigated by setting $\Delta\eta_0(\zeta, \eta) = 1$ in the inversion on the $N_\zeta = 10$ grid with the Manning's friction law and the fixed-endpoints scheme. Table 1 indicates that the statistics of the predicted water depth and total head are virtually indistinguishable from the ones with the variable $\Delta\eta_0$. There is a very simple explanation for this counterintuitive result. The reason is that the largest deviation of the geometric factor from $\Delta\eta_0 = 1$ occurs

near the banks, where it is multiplied by a power of the velocity field [see (8), (10), (14), and (16)], that is, a function that decreases very rapidly to zero near the banks.

The inversion based on the fixed endpoints scheme with the Manning's friction was also repeated on finer and coarser curvilinear grids with $N_\zeta = 20$ and $N_\zeta = 5$ cross-channel steps, respectively. The total head and water depth statistics shown in Table 1 suggest that the
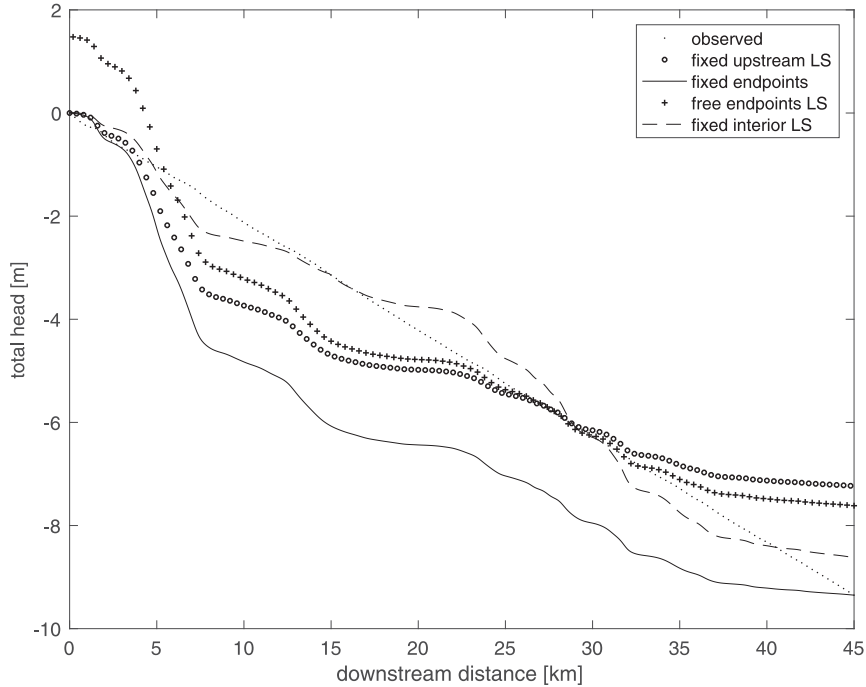
FIG. 12. Predicted and measured total head for the Columbia River at 0500 PDT 8 Oct 2011, offset by the measured total head at the upstream end.

inversion results are robust and do not depend significantly on the resolution for grids with cross-channel cells in the range of $N_\zeta = 5$–20. The counterintuitive increase of the R^2 value for coarser grid $N_\zeta = 5$ reflects the fact that the first interior node of the coarser grid is farther away from the problematic bank regions.

b. Columbia River: Variable discharge

We now turn our attention to the Columbia River data, where the assumption of steady flow is violated and the discharge is no longer constant in time or space. The main goal of this section is to investigate whether steady-state dynamics could be used to estimate bathymetry when the input data are unsteady.

We begin with the 0500 PDT data for which the PNNL hindcast simulations (Fig. 7) suggest that the discharge decreases only slightly from 1800 to $1700 \, \mathrm{m^3 \, s^{-1}}$ along the considered reach downstream of ADCP transect T16. For the Columbia River tests, we used primarily a curvilinear grid with an along-channel grid step of 100 m and $N_\zeta = 20$ steps in the cross-stream direction; the latter results in a 40-m cross-stream grid step where the river is the widest (~800 m wide). These grid steps are comparable with the grid size of the velocity data. For the bottom friction, we used a Manning's $n = 0.026$ that was obtained in calibration simulations over a discharge range $850 < Q < 8500 \, \mathrm{m^3 \, s^{-1}}$ (Richmond and Perkins

2009), consistent with the discharge conditions at the considered reach (see Figs. 6 and 7).

The predicted total head with the Manning's friction model is compared to the observed total head in Fig. 12. The two LS schemes (fixed upstream and free endpoints) again provided a much better approximation to the observed total head compared to the fixed-endpoints scheme. However, the best approximation to the observed total head is provided by a third LS scheme that fixes the predicted total head to the observed one at an interior point corresponding to a downstream distance of 15 km and leaves the upstream and downstream ends free; this scheme will be referred to as *fixed interior LS*. Other choices of the interior origin point (e.g., 10, 22, and 30 km) resulted in less accurate LS fits to the total head. Unlike the previous LS schemes, which assume a single discharge value for the entire domain, the fixed interior LS scheme uses two discharge values to independently minimize the total head error upstream and downstream of the interior origin point. The purpose of this scheme is to test whether a piecewise constant discharge profile would provide a better approximation to the observed spatially variable discharge. Table 2 shows that the fixed interior LS scheme provides the best fit to the observed total head with an rms error of 39 cm and $R^2 = 0.98$. Unfortunately, this scheme grossly under predicts the discharge downstream of the fixed interior

TABLE 2. Inversion statistics for the 0500 PDT 8 Oct 2011 Columbia River data when the discharge range was $1700 < Q < 1800 \, \text{m}^3 \, \text{s}^{-1}$. For the interior origin LS scheme the upstream discharge is followed by the downstream discharge.

Minimization scheme	N_ζ	Predicted discharge ($\text{m}^3 \, \text{s}^{-1}$)	Total head (m)			Thalweg depth (m)			2D depth (m)		
			Bias	rms	R^2	Bias	rms	R^2	Bias	rms	R^2
Free endpoints LS	20	1395	0	0.90	0.89	−0.56	1.49	0.64	0.77	2.26	0.59
Fixed endpoints	20	1368	−1.66	0.90	0.52	−0.67	1.48	0.63	0.72	2.27	0.60
Fixed upstream LS	20	1659	−0.22	1.04	0.85	0.55	1.68	0.56	1.23	2.20	0.55
Fixed interior LS	20	2243	0.03	0.39	0.98	−1.22	2.28	0.05	0.58	2.65	0.48
		931									
Free endpoints LS[a]	20	1045	0	0.76	0.92	−1.60	1.50	0.32	0.09	2.47	0.57
Fixed endpoints	20	1025	−1.47	0.76	0.63	−1.70	1.50	0.28	0.05	2.49	0.56
Fixed upstream LS[a]	20	1288	−0.21	0.90	0.88	−0.48	1.55	0.63	0.49	2.32	0.60
Fixed interior LS[a]	20	1863	0.02	0.34	0.98	−1.91	2.93	−0.73	0.08	2.94	0.38
		677									
Fixed upstream LS[b]	20	1644	−0.22	1.03	0.85	0.45	1.64	0.59	1.20	2.21	0.55
Fixed upstream LS	10	1779	−0.21	1.03	0.85	0.94	1.72	0.47	1.36	2.14	0.54

[a] Minimization schemes using the Darcy friction model instead of the Manning friction.

[b] Minimization that did not use the geometric correction to the total head slope.

point ($\eta = 15 \, \text{km}$), as the estimated $Q = 931 \, \text{m}^3 \, \text{s}^{-1}$ is significantly below the range of $1750 > Q > 1700 \, \text{m}^3 \, \text{s}^{-1}$ predicted in Fig. 7. The fixed interior LS scheme also overpredicts the observed discharge in the upstream part ($\eta < 15 \, \text{km}$) by about 30%.

The predicted depth error along the thalweg plotted in Fig. 13a shows that the single-discharge minimization schemes tend to underestimate the depth upstream of $\eta = 15 \, \text{km}$ and to overestimate downstream of that location. This behavior of the single-discharge schemes provided further motivation for attempting the piecewise constant discharge approximation. Figure 13a also shows that the fixed interior LS scheme reverses the behavior of the single-discharge schemes, but unfortunately the magnitude of the corrections is too large, resulting in larger depth errors upstream and downstream of $\eta = 15 \, \text{km}$. This result is reflected (Table 2) in the much larger bias and rms thalweg depth errors and the very poor $R^2 = 0.05$. The thalweg depth statistics in Table 2 suggest that, among all four inversions based on the Manning friction law, the free-endpoints LS scheme provides the most accurate depth prediction with a bias of −56 cm, an rms error of 1.49 m, and $R^2 = 0.64$. The same conclusion is also obtained from the scatterplots in Figs. 13b–d, where the depths predicted with the free-endpoints LS scheme are most tightly distributed around the straight line. However, the scheme that most closely matches the observed discharge while providing similar thalweg depth error statistics is the fixed upstream LS. The spatial distribution of the water depth predicted with the fixed upstream LS scheme is shown in Fig. 14. The map indicates that the inversion provides a good approximation to the observed water depth patterns in most of the domain except in the deep

region located 10 mi (~16 km) from the upstream end (Easting = 319 000 m). The 2D depth error statistics of the predicted depth in Fig. 14 are found to have a bias of 1.23 m, an rms error of 2.2 m, and $R^2 = 0.55$. This rms depth error is comparable to the 1.96-m error obtained in adjoint-based inversions with the same velocity measurements (Almeida et al. 2018). We should note that the latter approach consistently underestimated the maximum depth in the considered Columbia River reach by almost 30%. No such bias was found in the present approach, which slightly overestimates the largest depths (see Fig. 13c). Our rms depth error is about 15% of the maximum depth, which is also comparable to the Kootenai River error statistic found in section 4a.

Next, we investigated the sensitivity of the Columbia River inversions to the assumed bottom friction law, the geometric correction to the total head slope, and the resolution of the streamline-following grid. For the inversions with the Darcy bottom friction, we determined C_D from (11) using $n = 0.026$ and the observed mean thalweg depth $h_{\text{TW}} = 6.42 \, \text{m}$. The data in Table 2 indicate that the inversions based on the Darcy friction model again significantly underpredict the discharge, resulting in thalweg depths with much larger bias compared to the respective inversions with the Manning's friction law. Table 2 also shows that setting the metric factor $\Delta \eta_0(\zeta, \eta) = 1$ has little effect on the depth and discharge statistics of the predictions of the fixed upstream LS scheme. Similarly, we found that using a coarser grid with $N_\zeta = 10$ did not significantly change the results. We finally note that qualitatively similar results are obtained for the 0300 PDT velocity and water surface elevation data (Table 3). The main difference in the
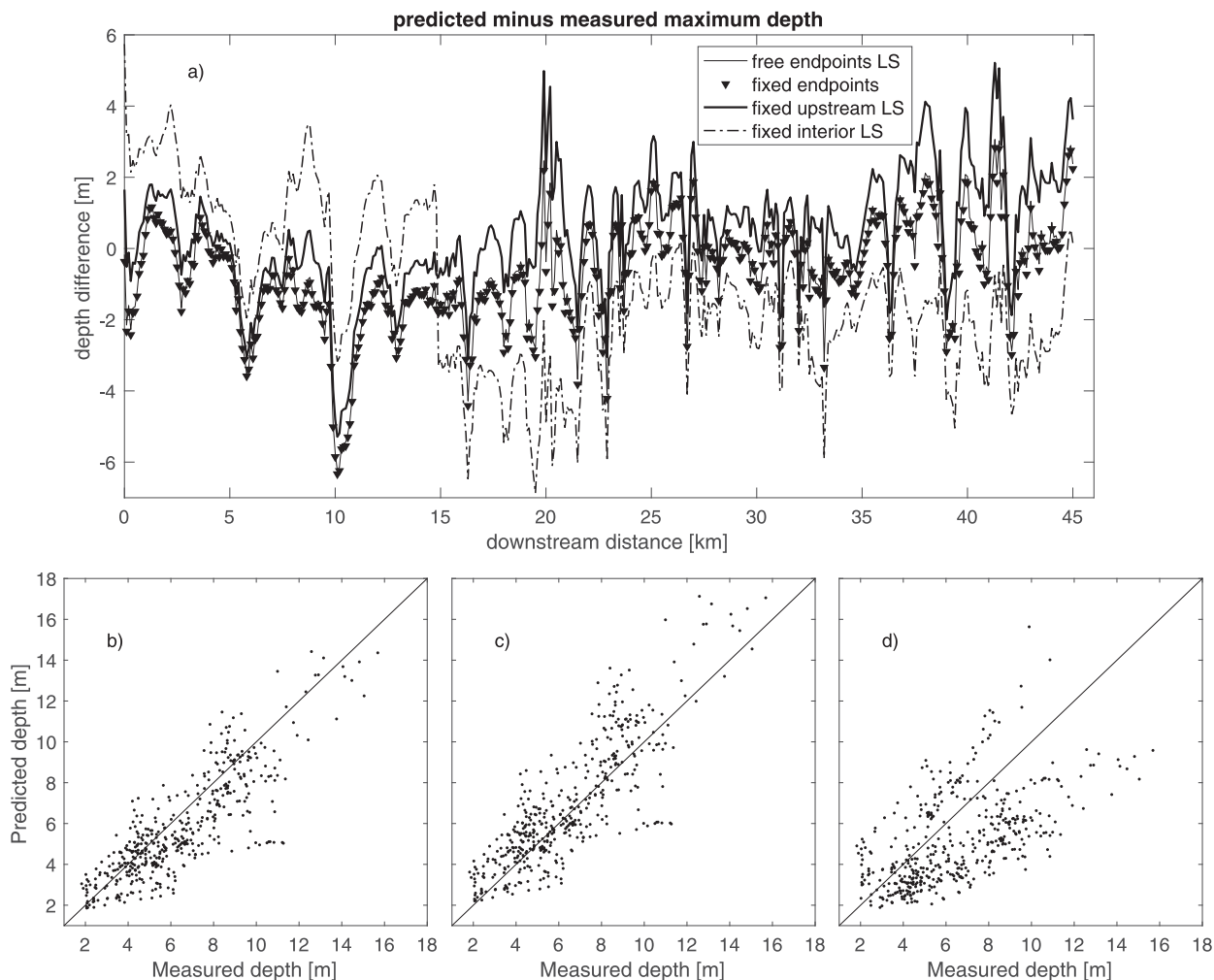
FIG. 13. (a) Difference between predicted and measured thalweg water depth for the Columbia River site. (bottom) Predicted thalweg depths (dots) vs measured depths for the different minimization schemes: (b) free-endpoints LS (fixed endpoints is similar to this one and not shown), (c) fixed upstream LS, (d) fixed interior LS.

0300 PDT inversion results was a larger bias in the estimated discharge. However, the predicted thalweg depth with the fixed upstream LS and Manning's friction law had a smaller bias error of -25 cm and better $R^2 = 0.69$ (Table 3). Examination of the 0300 PDT thalweg depth predictions (not shown) reveals similar underprediction of the depth for $\eta < 15$ km as in Fig. 13a but much closer prediction of the depth for $\eta > 15$ km.

The previous 2D depth inversion approaches and the one developed here require as an input the reach-wise average value of the ratio of the surface to depth-averaged velocity in order to convert the measured surface velocity into a depth-averaged one. Our ADCP measurements for the Columbia River and the meander reach of the Kootenai River suggest that the velocity ratio typically does not deviate more than a few percent from the theoretical value of 0.85, except in shallower

environments, such as the braided reach of the Kootenai River. When measurements of the velocity ratio are not available, the uncertainty in the predicted discharge and depth can be related to the uncertainty in the velocity ratio using the velocity–slope relationship in (12) and (13). For example, a large 5% uncertainty in the depth-averaged velocity would translate into a 12.5% uncertainty in the respective discharge estimate. A further reduction of the velocity ratio uncertainty can be achieved by combining the present approach with remote sensing measurements of the velocity ratio (Johnson and Cowen 2017).

Another important issue for the practical application of bathymetry inversion is identifying the spatial boundaries of reaches where the bottom friction is uniform and can be represented by a single parameter. In the examples considered here, the uniform bottom
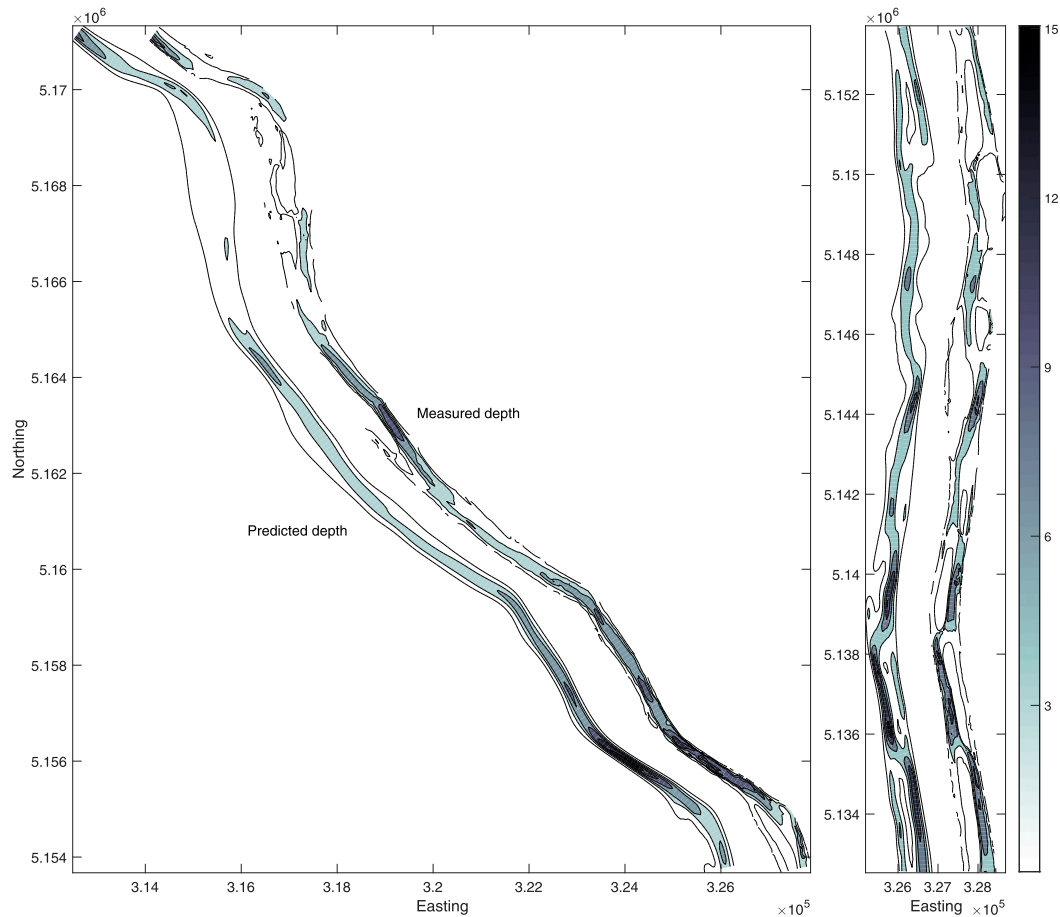
FIG. 14. Predicted and measured water depth map (blue shading) for the Columbia River at 0500 PDT 8 Oct 2011, using the fixed upstream LS method. The measured-depth map has an easting offset of 1600 m. Upstream is at the top-left corner of the left panel. The bottom-right corner of the left panel continues at the top of the right panel.

roughness reaches of the Kootenai and Columbia Rivers were identified in previous forward calibration simulations (e.g., McDonald et al. 2010; Richmond and Perkins 2009). However, such forward simulations require knowledge of the bathymetry and cannot be used for operational application of bathymetry inversion. In this regard, we would like to point out that our velocity–elevation relationships [see (9) and (15)] can also be used to identify uniform friction reaches from the measured velocity and surface elevation data when the discharge is approximately steady. For example, when the measured surface elevation is plotted as a function of the velocity integral in (9) and (15), reaches with uniform bottom friction will appear on the resulting graph as straight lines with distinct slope proportional to the local C_D. An alternative method to identify hydraulically distinct reaches using only measurements of the river sinuosity and the water surface elevation profile was also recently developed by Frasson et al. (2017)

using simulated SWOT altimeter data for the Sacramento and Po Rivers.

5. Conclusions

We developed an inverse modeling methodology to estimate river discharge and water depth based on measurements of the surface velocity and water surface elevation, and analytical velocity–depth and velocity–slope relationships derived from the steady momentum and mass conservation equations in streamline-following coordinates. The model skill and the limitations of the steady-state assumption were tested using several datasets with variable degree of unsteadiness—a Kootenai River dataset where the conditions were fairly steady and two Columbia River datasets with moderately unsteady discharge variation. The model results were found to be fairly insensitive to varying the grid resolution in the range of 5–20 grid steps across the channel width and to the

TABLE 3. Inversion statistics for the 0300 PDT 8 Oct 2011 Columbia River data when the discharge range was $1500 < Q < 1850 \, \mathrm{m^3 \, s^{-1}}$. For the interior origin LS scheme, the upstream discharge is followed by the downstream discharge.

Minimization scheme	N_ζ	Predicted discharge ($\mathrm{m^3 \, s}$)	Total head (m)			Thalweg depth (m)			2D depth (m)		
			Bias	rms	R^2	Bias	rms	R^2	Bias	rms	R^2
Free endpoints LS	20	1060	0	0.84	0.90	−1.23	1.33	0.54	0.50	2.33	0.60
Fixed endpoints	20	1044	−1.62	0.84	0.55	−1.31	1.32	0.51	0.46	2.34	0.60
Fixed upstream LS	20	1260	−0.22	0.99	0.86	−0.25	1.45	0.69	0.91	2.22	0.59
Fixed interior LS	20	1627	0.03	0.47	0.97	−1.65	1.90	0.11	0.38	2.58	0.52
		770									
Free endpoints LS[a]	20	749	0	0.72	0.93	−2.37	1.40	−0.08	−0.20	2.61	0.52
Fixed endpoints[a]	20	735	−1.45	0.72	0.65	−2.45	1.41	−0.13	−0.23	2.62	0.51
Fixed upstream LS[a]	20	920	−0.21	0.86	0.89	−1.45	1.36	0.44	0.14	2.44	0.58
Fixed interior LS[a]	20	1252	0.03	0.42	0.98	−2.84	2.48	−1.01	−0.31	2.94	0.38
		531									
Fixed upstream LS[b]	20	1246	−0.22	0.99	0.86	−0.35	1.42	0.70	0.88	2.23	0.59
Fixed upstream LS	10	1315	−0.22	0.99	0.86	−0.02	1.45	0.71	0.99	2.16	0.59

[a] Minimization schemes using the Darcy friction model instead of the Manning friction.
[b] Minimization that did not use the geometric correction to the total head slope.

geometric corrections of the water slope associated with the channel curvature. In all tests (Tables 1–3), we found that the Manning's friction parameterization of the bottom drag resulted in significantly better estimates of the discharge and water depth compared to the Darcy friction. The latter would typically underestimate the measured discharge by approximately 10% in the Kootenai River tests and up to 45% in the Columbia River tests. Thus, the conclusions made below pertain only to inversions using the Manning's friction parameterization. In the Kootenai River case, all three total head minimization schemes resulted in similar virtually unbiased thalweg depths with rms errors of about 0.60 m and $R^2 = 0.60$, total head profiles with rms errors less than 0.04 m, and predicted discharge values that matched the observed $Q = 213 \, \mathrm{m^3 \, s^{-1}}$ to within 5%.

Generally, we found larger discharge, total head, and thalweg depth biases in the Columbia River tests where the approximation of temporally and spatially uniform discharge is not formally valid. The best results were obtained for the 0500 PDT Columbia River data, with the fixed upstream LS minimization scheme yielding a discharge estimate of $1659 \, \mathrm{m^3 \, s^{-1}}$ that was close to the range of discharge variations $1800 > Q > 1700 \, \mathrm{m^3 \, s^{-1}}$ predicted in the PNNL forward simulations. The corresponding predicted thalweg depth and the total head profile were characterized with relatively low biases of 0.55 and −0.22 m, and rms errors of 1.68 and 1.04 m, respectively. For the 0300 PDT Columbia River data, the fixed upstream LS scheme provided thalweg depth and total head profile estimates with similar biases and rms errors, but the predicted discharge of $1260 \, \mathrm{m^3 \, s^{-1}}$ was significantly smaller that the discharge variations of $1800 > Q > 1600 \, \mathrm{m^3 \, s^{-1}}$ predicted in the corresponding PNNL simulation. We attribute this larger mismatch to the inability of our steady-state model to capture the larger temporal and spatial discharge variability in the 0300 PDT conditions. Future work should focus on extending the present analytical inversion approach by including the time dependence and along-channel variability in the mass conservation balance, and stage-dependent Manning roughness in the momentum balance.

REFERENCES

Almeida, T. G., D.T. Walker, and A. M. Warnock, 2018: Estimating river bathymetry from surface velocity observations using variational inverse modeling, *J. Atmos. Oceanic Technol.*, **35**, 21–34, https://doi.org/10.1175/JTECH-D-17-0075.1.

Barton, G., 2004: Characterization of channel substrate and changes in suspended-sediment transport and channel geometry in white sturgeon spawning habitat in the Kootenai River near Bonners Ferry, Idaho, following the closure of Libby Dam. Version 1, USGS Water-Resources Investigations Rep. 03-4324, 24 pp., https://pubs.usgs.gov/wri/2003/4324/report.pdf.

Bennett, A. F., 2002: *Inverse Modeling of the Ocean and Atmosphere.* Cambridge University Press, 234 pp.

Bjerklie, D. M., S. L. Dingman, C. J. Vorosmarty, C. H. Bolster, and R. G. Congalton, 2003: Evaluating the potential for measuring river discharge from space. *J. Hydrol.*, **278**, 17–38, https://doi.org/10.1016/S0022-1694(03)00129-X.

Chen, W., and R. P. Mied, 2013: River velocities from sequential multispectral remote sensing images. *Water Resour. Res.*, **49**, 3039–3103, https://doi.org/10.1002/wrcr.20267.

Coleman, A. M., K. B. Larson, D. L. Ward, and J. W. Lettrick, 2010: Development of a high-resolution bathymetry dataset for the Columbia River through the Hanford Reach. Pacific Northwest National Laboratory Rep. PNNL-19878, 72 pp., https://doi.org/10.2172/1000818.

Desai, S., 2018: Surface Water and Ocean Topography Mission (SWOT) Project: Science requirements document. Doc. JPL D-61923, 29 pp., http://swot.jpl.nasa.gov/docs/D-61923_SRD_Rev_B_20181113.pdf.

Dugan, J. P., S. P. Anderson, C. C. Piotrowski, and S. B. Zuckerman, 2013: Airborne infrared remote sensing of riverine currents. *IEEE Trans. Geosci. Remote Sens.,* **52**, 3895–3907, https://doi.org/10.1109/TGRS.2013.2277815.

Frasson, R. P. M., and Coauthors, 2017: Automated river reach definition strategies: Applications for the Surface Water and Ocean Topography Mission. *Water Resour. Res.*, **53**, 8164–8186, https://doi.org/10.1002/2017WR020887.

Garambois, P.-A., and J. Monnier, 2015: Inference of effective river properties from remotely sensed observations of water surface. *Adv. Water Resour.*, **79**, 103–120, https://doi.org/10.1016/j.advwatres.2015.02.007.

Gessese, A., and M. Sellier, 2012: A direct solution approach to the inverse shallow-water problem. *Math. Probl. Eng.*, **2012**, 417950, https://doi.org/10.1155/2012/417950.

Honnorat, M., J. Monnier, and F.-X. Le Dimet, 2009: Lagrangian data assimilations for river hydraulics simulations. *Comput. Visualization Sci.*, **12**, 235–246, https://doi.org/10.1007/s00791-008-0089-x.

Johnson, E. D., and E. A. Cowen, 2016: Remote monitoring of volumetric discharge employing bathymetry determined from surface turbulence metrics. *Water Resour. Res.*, **52**, 2178–2193, https://doi.org/10.1002/2015WR017736.

——, and ——, 2017: Remote determination of the velocity index and mean streamwise velocity profile. *Water Resour. Res.*, **53**, 7521–7535, https://doi.org/10.1002/2017WR020504.

Landon, K. C., G. W. Wilson, H. T. Ozkan-Haller, and J. H. MacMahan, 2014: Bathymetry estimation using drifter-based velocity measurements on the Kootenai River, Idaho. *J. Atmos. Oceanic Technol.*, **31**, 503–514, https://doi.org/10.1175/JTECH-D-13-00123.1.

McDonald, R., J. Nelson, V. Paragamian, and G. Barton, 2010: Modeling the effect of flow and sediment transport on white sturgeon spawning habitat in the Kootenai River, Idaho. *J. Hydraul. Eng.*, **136**, 1077–1092, https://doi.org/10.1061/(ASCE)HY.1943-7900.0000283.

Rantz, S. E., 1982: Measurements of stage and discharge. Vol. 1, Measurements and computation of streamflow, USGS Water Supply Paper 2175, 284 pp.

Richmond, M. C., and W. A. Perkins, 2009: Efficient calculation of dewatered and entrapped areas using hydrodynamics modeling and GIS. *Environ. Modell. Software*, **24**, 1447–1456, https://doi.org/10.1016/j.envsoft.2009.06.001.

Simeonov, J. A., K. T. Holland, J. Calantoni, and S. P. Anderson, 2013: Calibrating discharge, bed friction, and datum bias in hydraulic models using water level and surface current observations. *Water Resour. Res.*, **49**, 8026–8038, https://doi.org/10.1002/2013WR014474.

Yoon, Y., M. Durand, C. J. Merry, E. A. Clark, K. M. Andreadis, and D. E. Alsdorf, 2012: Estimating river bathymetry from data assimilation of synthetic SWOT measurements. *J. Hydrol.*, **464–465**, 363–375, https://doi.org/10.1016/j.jhydrol.2012.07.028.

Zaron, E. D., 2017: Recent developments in bottom topography mapping using inverse methods. *Data Assimilation for Atmospheric, Oceanic and Hydrologic Applications*, S. K. Park and L. Xu, Eds., Vol. III, Springer, 241–258, https://doi.org/10.1007/978-3-319-43415-5_11.

——, M.-A. Pradal, P. D. Miller, A. F. Blumberg, N. Georgas, W. Li, and J. M. Cornuelle, 2011: Bottom topography mapping via nonlinear data assimilation. *J. Atmos. Oceanic Technol.*, **28**, 1606–1623, https://doi.org/10.1175/JTECH-D-11-00070.1.